Injection locking of a semiconductor double-quantum-dot micromaser

Y.-Y. Liu,[1] J. Stehlik,[1] M. J. Gullans,[2,3] J. M. Taylor,[2,3] and J. R. Petta[1]
[1]*Department of Physics, Princeton University, Princeton, New Jersey 08544, USA*
[2]*Joint Quantum Institute, National Institute of Standards and Technology, Gaithersburg, Maryland 20899, USA*
[3]*Joint Center for Quantum Information and Computer Science, University of Maryland, College Park, Maryland 20742, USA*
(Received 17 August 2015; published 2 November 2015)

The semiconductor double-quantum-dot (DQD) micromaser generates photons through single-electron tunneling events. Charge noise couples to the DQD energy levels, resulting in a maser linewidth that is 100 times larger than the Schawlow-Townes prediction. We demonstrate linewidth narrowing by more than a factor of 10 using injection locking. The injection locking range is measured as a function of input power and is shown to be in excellent agreement with the Adler equation. The position and amplitude of distortion sidebands that appear outside of the injection locking range are quantitatively examined. Our results show that this unconventional maser, which is impacted by strong charge noise and electron-phonon coupling, is well described by standard laser models.

DOI: 10.1103/PhysRevA.92.053802 PACS number(s): 42.60.Fc, 73.21.La, 73.23.Hk, 84.40.Ik

I. INTRODUCTION

Masers were instrumental in the birth of the laser [1,2] and are now employed as frequency standards [3,4] and low-noise amplifiers [5]. The most widely used masers operate in a vacuum environment with atoms [3] or electrons [6,7], but solid-state masers are also common [8–11]. Due to charge fluctuations, solid-state masers and lasers typically have much broader linewidths than their vacuum counterparts; therefore, to harness the full potential of these solid-state devices, it is important to stabilize the emission frequency.

Injection locking is a common method for narrowing the linewidth of a laser. With injection locking, laser emission is stabilized by the injection of an input tone that results in stimulated emission at the frequency of the injected tone. Frequency locking of oscillators has a rich history, extending back to Huygens in 1666, who observed that two initially unsynchronized clocks would eventually synchronize due to mechanical vibrations transmitted via a common beam [12]. Since then, frequency locking has been observed in systems ranging from fireflies [13], to spin-transfer torque oscillators [14], and matter waves of a Bose gas [15]. For optical lasers, injection locking was first observed by Stover and Steier [16] and is now commonly used to improve the coherence of lasers [17].

In this paper we demonstrate injection locking of the recently discovered semiconductor double-quantum-dot (DQD) micromaser. The DQD micromaser is driven by single-electron tunneling events between discrete zero-dimensional electronic states [18]. A free-running emission linewidth of 34 kHz was measured, nearly 100 times larger than the Schawlow-Townes (ST) prediction [1]. Time-series analysis of the emitted signal indicates the maser output is fluctuating as a function of time. These fluctuations are believed to be due to charge noise, which electrostatically couples to the DQD energy levels and results in significant broadening of the emission peak.

Here we show that the emission linewidth can be narrowed by more than a factor of 10 using injection locking. For the case when the input tone $f_{\rm in}$ is detuned from the free-running maser frequency by several linewidths, the maser emission frequency is "pulled" by and eventually locked to the input tone with increasing input power $P_{\rm in}$. The frequency range over which the maser can be injection locked $\Delta f_{\rm in}$ increases with $P_{\rm in}$ following the power-law relation $\Delta f_{\rm in} \propto \sqrt{P_{\rm in}}$ predicted by Adler [19]. We also investigate the dynamics of the maser just outside of the injection locking regime, where the frequency pull is appreciable and leads to distortion sidebands in the emission spectrum. The emission powers and positions of the sidebands are in excellent agreement with theoretical predictions [12,20]. These measurements indicate that the DQD micromaser, which is driven by single-electron tunneling events, follows predictions from conventional laser theory and can be considerably improved using injection locking effects.

II. DOUBLE-QUANTUM-DOT MICROMASER

The DQD micromaser is fabricated in the circuit quantum electrodynamics architecture (cQED) and consists of a superconducting transmission line resonator, two semiconductor DQDs that serve as the gain medium, and a voltage bias that generates population inversion [21]. The half-wavelength ($\lambda/2$) Nb coplanar waveguide resonator has a resonance frequency $f_c = 7880.6$ MHz [22–24]. The cQED architecture has been used to achieve strong coupling between microwave frequency photons and a superconducting qubit [22]. A variety of quantum dot devices have been integrated with microwave cavities [23–26].

The maser gain medium consists of two semiconductor DQDs, as illustrated in Fig. 1. Each DQD is fabricated by placing a single InAs nanowire across a predefined array of bottom gates [27]. Negative voltages are applied to the gates to selectively deplete the nanowire, forming a DQD [27,28]. Electronic confinement results in a discrete energy-level spectrum that can be electrically tuned [28,29]. In semiconductor DQDs the electric dipole moment $d \sim 1000ea_0$, which interacts with the oscillating cavity voltage $V_{\rm cavity}$ and results in a charge-cavity interaction rate $g_c/2\pi \approx 30$ MHz [18,23–25,30,31]. Here e is the electronic charge and a_0 is the Bohr radius.

A source-drain bias, $V_{\rm SD} = 2$ mV $= (\mu_{\rm D} - \mu_{\rm S})/|e|$, is applied to give a preferred direction for electron flow, where $\mu_{\rm S}(\mu_{\rm D})$ is the chemical potential of the source(drain). As shown in Fig. 1, single-electron tunneling is only allowed

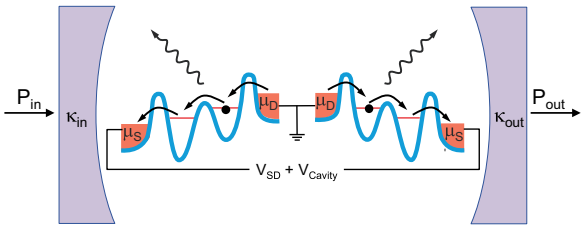

FIG. 1. (Color online) Schematic of the DQD micromaser. Two DQDs are coupled to a high-quality factor microwave cavity with input (output) coupling rates κ_{in} (κ_{out}). A source-drain bias voltage V_{SD} results in single-electron tunneling through the DQDs and leads to photon emission into the cavity mode.

when the DQD energy levels are arranged such that an electron can tunnel downhill in energy; otherwise current flow is blocked due to Coulomb blockade [28]. Starting with an empty DQD (see left DQD in Fig. 1), a single electron first tunnels from the drain to the right dot. This tunneling event is followed by an interdot charge transition and subsequent tunneling of the electron from the left dot to the source. The source-drain bias effectively repumps the higher energy level in the DQD and generates conditions for population inversion. The interdot charge transition results in microwave frequency photon emission [18,21].

The DQD micromaser is in some ways similar to a quantum cascade laser (QCL). In a QCL, current flows through a precisely engineered quantum well structure and results in the cascaded emission of photons whose frequency is set by the quantum well layer thicknesses [32]. In comparison, photons in the DQD micromaser are generated by single-electron tunneling between electrically tunable DQD energy levels. While electrical control allows for *in situ* tuning of the gain medium, it also means that the energy-level separation will be susceptible to charge noise. The root-mean-square charge noise $\sigma_\epsilon/h = 10$ GHz is typically much larger than $g_c/2\pi \approx 30$ MHz and the cavity linewidth $\kappa_{tot}/2\pi \approx 3$ MHz [18,23–26]. Charge noise will drive the DQDs out of resonance with the cavity, making it difficult to reach the strong-coupling regime [33–35]. In terms of maser performance, charge fluctuations adversely impact emission frequency and power stability [21].

III. EXPERIMENTAL RESULTS

We now present experimental data obtained on the semiconductor DQD micromaser. In Sec. III A we briefly review measurements of the DQD micromaser that examined the amplification of an input tone and the photon statistics in free-running mode (i.e., cavity emission in the absence of an input tone) [21]. In Sec. III B we present new results showing that the maser emission can be injection locked by driving the input port of the cavity with a corresponding reduction in the emission linewidth. The injection locking range is measured as a function of input power and shown to be in good agreement with standard laser theory. Section III C examines the frequency pull and distortion sidebands that appear outside of the locking range. Detailed analysis of the sidebands also yields excellent agreement with theoretical predictions.

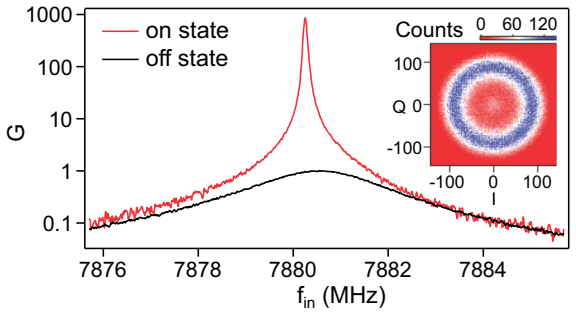

FIG. 2. (Color online) Power gain $G = C P_{out}/P_{in}$ plotted as a function of f_{in} with the DQDs configured in Coulomb blockade with no current flow (off state) and with current flowing through the DQDs (on state). In the on state, the peak gain $G_p \sim 1000$ and the linewidth is dramatically narrowed, suggestive of a transition to a masing state. Inset: IQ histogram of the output field measured in the on state and with no input tone applied to the cavity. The donut shape is indicative of above-threshold maser action [12,21].

A. Free-running maser characterization

The maser is first characterized by driving the input port of the cavity at frequency f_{in} and power P_{in}. Cavity power gain is defined as $G = C P_{out}/P_{in}$, where P_{out} is the power exiting the cavity. The normalization constant C is defined such that the peak power gain $G_p = 1$ when both DQDs are configured in Coulomb blockade (referred to as the "off state"). Figure 2 shows G as a function of f_{in} with $P_{in} = -120$ dBm. The black curve is the cavity response in the off state [21]. Fitting the gain to a Lorentzian, we extract the cavity center frequency $f_c = 7880.6$ MHz and linewidth $\kappa_{tot}/2\pi = 2.6$ MHz. Here $\kappa_{tot} = \kappa_{in} + \kappa_{out} + \kappa_{int}$. $\kappa_{in}(\kappa_{out})$ is the decay rate through the input(output) port and κ_{int} is the photon loss rate through other channels. The red curve shows G as a function of f_{in} when current is flowing through both DQDs (defined as the "on state"). Here the cavity response is sharply peaked at $f_{in} = 7880.25$ MHz, yielding $G_p \sim 1000$ with a FWHM $\Gamma = 0.07$ MHz, suggestive of a transition to an above-threshold maser state.

Above-threshold maser action is confirmed by measuring the statistics of the output field [21]. These measurements are performed in free-running mode (with no input tone applied). The output signal is amplified and demodulated to yield the in-phase (I) and quadrature-phase (Q) components, which are sampled at a rate of 1 MHz. The results from 400,000 individual (I, Q) measurements are shown in the two-dimensional histogram plotted in the inset of Fig. 2(b). The IQ histogram has a donut shape that is consistent with a stable oscillator; however, the amplitude fluctuations are much larger than expected. Time-series analysis of the free-running emission signal suggests that large charge fluctuations are impacting the emission stability [21]. It is therefore desirable to stabilize the output of the maser.

B. Injection locking the semiconductor DQD micromaser

We now demonstrate injection locking of the maser by measuring the power spectral density of the emitted radiation $S(f)$ as a function of the power P_{in} of the input tone. The main panel of Fig. 3(a) shows $S(f)$ as a function of P_{in} with $f_{in} =$

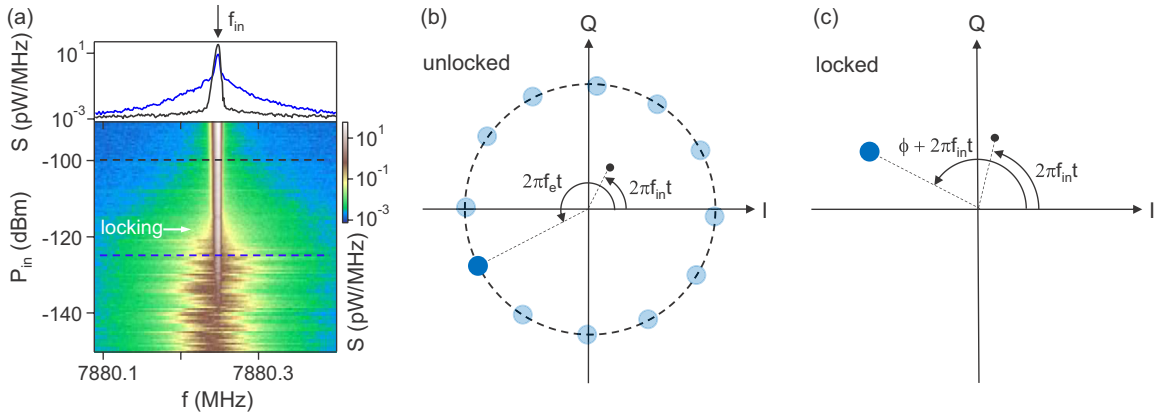

FIG. 3. (Color online) (a) Power spectrum of the emitted radiation $S(f)$ plotted as a function of $P_{\rm in}$. The cavity input frequency $f_{\rm in} = 7880.25$ MHz is close to the free-running maser emission frequency $f_{\rm e} = 7880.25 \pm 0.03$ MHz. Note the significant fluctuations in $f_{\rm e}$ for $P_{\rm in} < -120$ dBm. The maser linewidth narrows with increasing $P_{\rm in}$ due to injection locking. The upper panel shows $S(f)$ for $P_{\rm in} = -125$ dBm (blue) and $P_{\rm in} = -100$ dBm (black), indicated by the dashed lines in the main panel. (b) Phasor diagram of the maser output in the unlocked configuration. Here the cavity field is a combination of the free-running maser emission at frequency $f_{\rm e}$ and the cavity input tone at $f_{\rm in}$. In this configuration the phase of the maser is fluctuating relative to the input tone. (c) Schematic illustration of the cavity field in the injection locked state. To within a relative phase ϕ, the maser emission is locked to the input tone.

7880.25 MHz set near the free-running emission frequency $f_{\rm e}$. Line cuts through the data are shown in the upper panel for $P_{\rm in} = -125$ dBm (blue curve) and -100 dBm (black curve). For negligible input powers ($P_{\rm in} < -140$ dBm) the power spectrum exhibits a broad peak near $f_{\rm e} = 7880.25$ MHz. For a given value of $P_{\rm in}$, the emission peak typically has a FWHM of $\Gamma = 34$ kHz. For $P_{\rm in} < -125$ dBm, charge noise causes the emission peak to significantly wander in the frequency range 7880.25 ± 0.03 MHz. In this configuration the relative phases of the input tone and the maser emission are unlocked, as illustrated in Fig. 3(b). As $P_{\rm in}$ is increased, the photon number in the cavity at $f_{\rm in}$ increases, resulting in increased stimulated emission. With $P_{\rm in} > -125$ dBm, the broad tails of the emission peak are suppressed and the spectrum begins to narrow. The free-running maser emission is eventually locked to the input tone at around $P_{\rm in} = -115$ dBm. Now the large fluctuations that were observed in the absence of an input tone are suppressed and $\Gamma < 3$ kHz [36]. The linewidth is reduced by more than a factor of 10 compared to the free-running case and indicates phase stabilization, as illustrated in Fig. 3(c).

Although our minimum linewidth resolution is set by technical limitations [36], we can estimate the fundamental linewidth limit for this device. Previous measurements of the output field indicated that the masing process intermittently shuts off due to large charge fluctuations [21]. During these off periods, the maser emission will cease to be injection locked to the input tone and will lose phase coherence. As a result, the linewidth will be limited by the inverse of the switching time τ_s. In Ref. [21], τ_s was observed to be roughly 500 μs, which sets the fundamental linewidth limit due to charge noise as $\Gamma \sim 1/\tau_s \approx 2$kHz. The linewidth prediction is comparable to our measurement resolution and is a factor of 10 smaller than the linewidth of the free-running maser, but still larger than the ST limit by the same factor. Further reductions of the linewidth will most likely require reducing charge noise in these devices.

Comparable effects are observed when $f_{\rm in} = 7880.60$ MHz, more than ten linewidths detuned from $f_{\rm e}$ (Fig. 4). With $P_{\rm in} < -140$ dBm, only the free-running emission peak is visible in $S(f)$. As $P_{\rm in}$ is further increased the injection tone becomes visible and the power spectrum is simply a sum of the free-running maser emission and the cavity input tone. When $P_{\rm in} \gtrsim -125$ dBm, distortion sidebands appear and the free-running emission peak is pulled towards the input tone. The maser abruptly locks to $f_{\rm in}$ when $P_{\rm in} = -102$ dBm, but the emission is still somewhat broad. The linewidth continues to narrow until $P_{\rm in} = -98$ dBm,

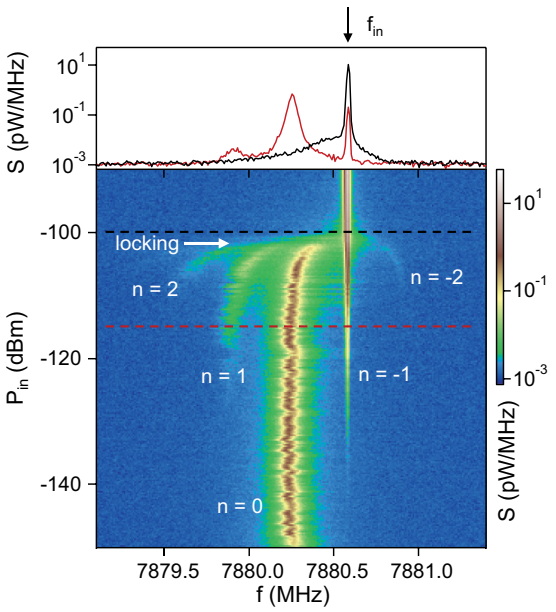

FIG. 4. (Color online) $S(f)$ plotted as a function of $P_{\rm in}$ with $f_{\rm in} = 7880.6$ MHz far detuned from $f_{\rm e}$. (Note the change in the x-axis scale relative to Fig. 3) The maser is injection locked when $P_{\rm in} > -102$ dBm. Distortion sidebands are clearly visible in the emission spectrum. Upper panel: $S(f)$ for $P_{\rm in} = -115$ dBm (red) and $P_{\rm in} = -100$ dBm (black), indicated by the dashed lines in the main panel.

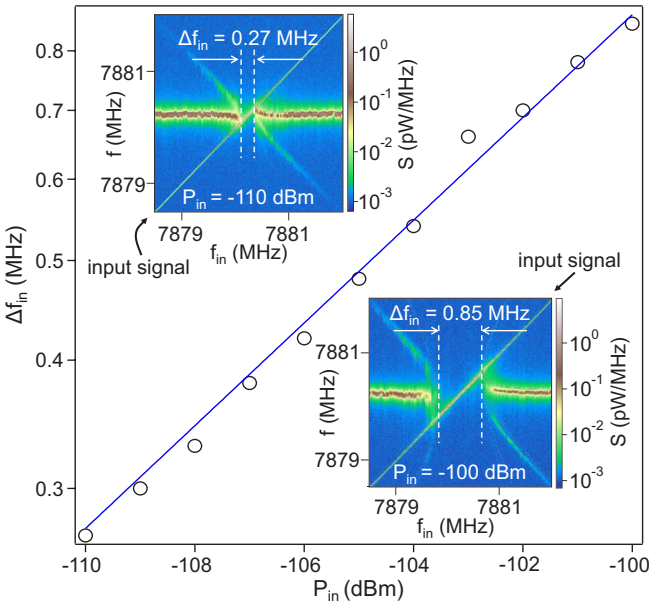

FIG. 5. (Color online) The frequency range over which the maser is injection locked, $\Delta f_{\rm in}$, increases with $P_{\rm in}$. The blue line is a fit to the power law $\Delta f_{\rm in} \propto \sqrt{P_{\rm in}}$ prediction of the Adler equation. Insets: $S(f)$ measured as a function of $f_{\rm in}$ with $P_{\rm in} = -110$ dBm (upper left) and $P_{\rm in} = -100$ dBm (lower right).

beyond which point the measured linewidth is limited by experimental factors [36]. The upper panel of Fig. 4 shows line cuts through the data, acquired at $P_{\rm in} = -115$ dBm (red curve) and $P_{\rm in} = -100$ dBm (black curve). The sidebands that are visible in $S(f)$ (marked $n = -2, -1, 0, 1$, and 2) are quantitatively analyzed in Sec. III C [12,20].

We next measure the frequency range over which the maser is injection locked. The upper inset of Fig. 5 shows a color-scale plot of $S(f)$ as a function of $f_{\rm in}$ measured with $P_{\rm in} = -110$ dBm. The input signal is visible in $S(f)$ and marked with an arrow for clarity. As seen in the data, $f_{\rm in}$ has little effect on the maser emission when it is far detuned from $f_{\rm e}$. As $f_{\rm in}$ is increased and brought closer to $f_{\rm e}$, frequency pulling is visible and emission sidebands appear. The maser then abruptly locks to $f_{\rm in}$ and remains locked to $f_{\rm in}$ over a frequency range $\Delta f_{\rm in} = 0.27$ MHz. The lower inset of Fig. 5 shows $S(f)$ as a function of $f_{\rm in}$, with $P_{\rm in} = -100$ dBm. Here the maser is injection locked over a larger range $\Delta f_{\rm in} = 0.85$ MHz. Similar to the upper inset, frequency pulling and sidebands are observed outside of the injection locking range. By repeating these measurements at different $P_{\rm in}$, we obtain the data shown in the main panel of Fig. 5, where $\Delta f_{\rm in}$ is plotted as a function of $P_{\rm in}$. The blue line in Fig. 5 is a fit to the power-law relation $\Delta f_{\rm in} = A_{\rm M}\sqrt{P_{\rm in}}$, with the measured prefactor $A_{\rm M} = (2.7 \pm 1.0) \times 10^6$ MHz/$\sqrt{\rm W}$, where the error bar is due to 3 dB of uncertainty in the transmission line losses.

The measured power-law relation can be compared with predictions from Adler's theory, which considers the maser dynamics in the rotating frame of the input tone by assuming that the input power is small compared to the free emission power [19]. We express the time-dependent complex cavity output field amplitude as

$$\alpha(t) = I(t) + i\,Q(t) = \sqrt{P_e}\,e^{2\pi i f_{\rm in} t + i\phi(t)}, \tag{1}$$

where P_e is the emitted power (assumed to be constant) and $\phi = \phi_{\rm e} - \phi_{\rm in}$ is the relative phase of the input field $\phi_{\rm in}$ and the emitted field $\phi_{\rm e}$. The relative phase follows the Adler equation:

$$\frac{d\phi}{dt} + 2\pi(f_{\rm in} - f_{\rm e}) = -2\pi\frac{\Delta f_{\rm in}}{2}\sin(\phi). \tag{2}$$

In the injection locking range $|f_{\rm in} - f_{\rm e}| < \Delta f_{\rm in}/2$, Eq. (2) has a static solution $\phi = \arcsin[2(f_{\rm e} - f_{\rm in})/\Delta f_{\rm in}]$. The emission phase is then locked to the input tone with $\phi \in (-\pi/2, \pi/2)$, which corresponds to the case illustrated in Fig. 3(c).

Adler's analysis shows that $\Delta f_{\rm in}$ is proportional to the amplitude of the input signal such that

$$\Delta f_{\rm in} = C_\kappa \frac{\kappa_{\rm tot}}{2\pi}\sqrt{P_{\rm in}/P_{\rm e}} \equiv A_{\rm T}\sqrt{P_{\rm in}}. \tag{3}$$

The cavity prefactor $C_\kappa = 2\sqrt{\kappa_{\rm in}\kappa_{\rm out}}/\kappa_{\rm tot}$ accounts for internal cavity losses and is obtained using cavity input-output theory [12]. Our microwave cavity is designed with $\kappa_{\rm in}/2\pi = \kappa_{\rm out}/2\pi = 0.39$ MHz. $\kappa_{\rm tot}/2\pi = 2.6$ MHz is directly extracted from the data in Fig. 2. These quantities yield $C_\kappa = 0.3$. The average emitted maser output power $P_{\rm e} \approx (2.5 \pm 1.9) \times 10^{-2}$ pW. Using these quantities we find the theoretical prefactor

$$A_{\rm T} = \frac{C_\kappa}{\sqrt{P_{\rm e}}}\frac{\kappa_{\rm tot}}{2\pi} = (4.9 \pm 1.7) \times 10^6\ {\rm MHz}/\sqrt{\rm W}.$$

We therefore find reasonable agreement between the data and the predictions from Adler's theory, considering the uncertainties in the transmission line losses.

C. Behavior outside of the injection locking range: Frequency pull and distortion sidebands

We now examine the behavior of the maser outside of the injection locking range, where the frequency pull is appreciable and distortion sidebands are visible. Figure 6(a) shows $S(f)$ as a function of $f_{\rm in}$ with $P_{\rm in} = -105$ dBm. Injection locking is observed over a frequency range $\Delta f_{\rm in} = 0.48$ MHz. Focusing on the region with $f_{\rm in} > 7880.5$ MHz, we observe one sideband for $f > f_{\rm e}$ and two sidebands for $f < f_{\rm e}$. For clarity, the emission peaks are labeled with the index n: $n = 0$ corresponds to the frequency-pulled maser emission peak, $n = -1$ corresponds to the input tone, and the other peaks are distortion sidebands. Figure 6(b) shows line cuts through the data at $f_{\rm in} = 7880.92$ MHz (upper panel) and $f_{\rm in} = 7880.60$ MHz (lower panel). When $f_{\rm in} = 7880.92$ MHz, the pulled emission peak $\bar{f}_{\rm e}$ ($n = 0$) is detuned from $f_{\rm in}$ by the beat frequency $f_{\rm b} = \bar{f}_{\rm e} - f_{\rm in}$. For this set of parameters we measure $f_{\rm b} = -0.68$ MHz. The $n = 1$ sideband is detuned from the $n = 0$ peak by $f_{\rm b}$. When $f_{\rm in} = 7880.60$ MHz, the $n = 2$ sideband is also visible. To allow for a quantitative comparison with theory, we analyze the spectra in Fig. 6(b) by fitting the sideband emission peaks to a Lorentzian line shape and the input tone to a Gaussian with a width of 10 kHz [36]. The integrated sideband powers $P_{\rm n}$ extracted from the fitting procedure are listed in Table I.

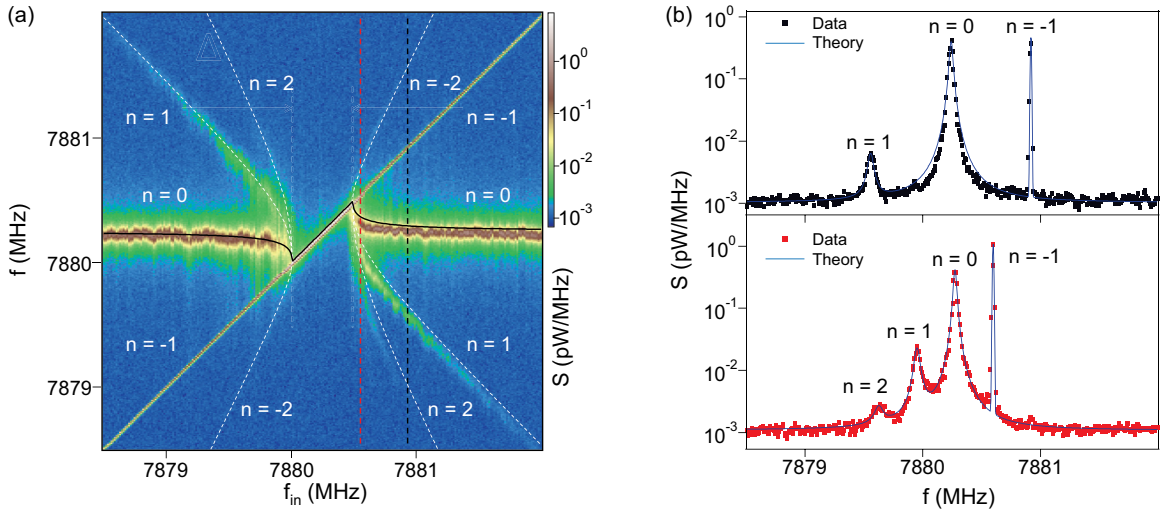

FIG. 6. (Color online) (a) $S(f)$ measured as a function of $f_{\rm in}$ with $P_{\rm in} = -105$ dBm. The black line overlaid on the data is the pulled frequency $\bar{f}_{\rm e}$ predicted by Adler's injection locking theory. The white dashed lines are the predicted sideband locations. (b) $S(f)$ for $f_{\rm in} =$ 7880.92 MHz (upper panel) and $f_{\rm in} = 7880.60$ MHz (lower panel), indicated by the dashed lines in (a). Solid lines are fits to $S(f)$.

To compare the data with theory, we seek a general solution for $\phi(t)$. In the limit of small $P_{\rm in}$, $\Delta f_{\rm in} \approx 0$ and $\phi(t) \approx 2\pi (f_{\rm e} - f_{\rm in})t$. In this case the cavity field can simply be considered as a sum of the free emission signal and the cavity input tone, as shown in Fig. 3(b). Outside of this limit, we solve the Adler equation analytically to find the cavity field

$$\alpha = \sqrt{P_{\rm e}} e^{2\pi i (f_{\rm in} + f_{\rm b})t} \left(\sum_{n=-\infty}^{\infty} a_n e^{2\pi i n f_{\rm b} t} \right). \tag{4}$$

The expansion coefficients a_n have been calculated by Armand [37]. The beat frequency is found self-consistently from this solution:

$$f_{\rm b} = (f_{\rm e} - f_{\rm in}) \sqrt{1 - \left(\frac{\Delta f_{\rm in}/2}{f_{\rm e} - f_{\rm in}} \right)^2}. \tag{5}$$

Given that $f_{\rm e}$ wanders in the frequency range 7880.25 ± 0.03 MHz, Eq. (5) predicts $f_{\rm b} = -0.63 \pm 0.03$ MHz at $f_{\rm in} = 7880.92$ MHz and, $f_{\rm b} = -0.25 \pm 0.03$ MHz at $f_{\rm in} = 7880.60$ MHz. These values are in general agreement with the measured $f_{\rm b}$ listed in Table I. The small discrepancy may be due to charge-noise-induced drift in $f_{\rm e}$.

Predicted sideband positions can be obtained by evaluating Eq. (4) in several different regimes. For the far-detuned case $|f_{\rm e} - f_{\rm in}| \gg \Delta f_{\rm in}$, higher-order harmonics are negligible and $a_0 \approx 1$. Equation (4) then simplifies to $\alpha = \sqrt{P_e} e^{2\pi i (f_{\rm in} + f_{\rm b})t}$, which represents the pulled emission peak at frequency $\bar{f}_e = f_{\rm in} + f_b$. First-order expansion of Eq. (4) in $\Delta f_{\rm in}$ yields $a_{\pm 1} \approx i \Delta f_{\rm in}/4(f_{\rm e} - f_{\rm in})$ [38]. When the detuning $|f_{\rm e} - f_{\rm in}|$ approaches $\Delta f_{\rm in}/2$, higher-order terms in Eq. (4) give rise to non-negligible expansion coefficients a_n, which results in higher-order sideband peaks at frequencies $f_n = \bar{f}_e \pm n f_b$ ($n = \pm 1, \pm 2, ...$). The predicted $\bar{f}_e$ is plotted as a black solid line in Fig. 6(a), and the predicted $n \neq 0$ sidebands are plotted as white dashed lines. Both the pulled emission peak and the location of the distortion sidebands are in good agreement with Adler's theory.

TABLE I. Distortion sideband parameters.

$f_{\rm in}$ (MHz)	7880.92	7880.60
$f_{\rm b}$ (MHz)	–0.68	–0.33
P_0 (pW)	2.1×10^{-2}	2.0×10^{-2}
P_1 (pW)	5.4×10^{-4}	1.8×10^{-3}
P_2 (pW)	NA	1.59×10^{-4}
P_1/P_0	2.7×10^{-2}	9.1×10^{-2}
P_2/P_0	NA	7.9×10^{-3}
$\lvert a_1/a_0 \rvert^2$	2.9×10^{-2}	1.0×10^{-1}
$\lvert a_2/a_0 \rvert^2$	NA	1.1×10^{-2}

The integrated sideband powers $P_{\rm n}$ can be compared with calculations from Armand [37], who found

$$a_{-1} = \frac{f_{\rm e} - f_{\rm in} - f_{\rm b} + i(\Delta f_{\rm in}/2)}{f_{\rm e} - f_{\rm in} + f_{\rm b} - i(\Delta f_{\rm in}/2)}.$$

Since the $n = -1$ sideband overlaps with the input tone, it cannot be resolved experimentally. $a_n = 0$ for $n \leqslant -2$,

$$a_0 = \frac{4(f_{\rm e} - f_{\rm in}) f_{\rm b}}{[f_{\rm e} - f_{\rm in} + f_{\rm b} - i(\Delta f_{\rm in}/2)]^2},$$

and for $n > 0$,

$$a_n = a_0 \left[\frac{(-f_{\rm e} + f_{\rm in} + f_{\rm b}) + i(\Delta f_{\rm in}/2)}{(f_{\rm e} - f_{\rm in} + f_{\rm b}) - i(\Delta f_{\rm in}/2)} \right]^n. \tag{6}$$

The predictions imply that the $n > 0$ sidebands are favored, an asymmetry that is consistent with the data in Fig. 6(b), as well as other laser systems [38,39].

We can now compare the measured sideband powers with the theoretical predictions. For the data shown in the upper panel of Fig. 6(b), we find $P_1/P_0 = 2.7 \times 10^{-2}$, which is very close to the value predicted by Eq. (6), $|a_1/a_0|^2 = 2.9 \times 10^{-2}$. The theoretical value is calculated by taking the measured beat frequency $f_{\rm b} = -0.68$ MHz, the measured $\Delta f_{\rm in} = 0.48$ MHz obtained with $P_{\rm in} = -105$ dBm, and $f_{\rm e} - f_{\rm in} = -0.72$ MHz determined from Eq. (5). Similarly, for the lower panel of Fig. 6(b), Adler's theory predicts ratios of $|a_1/a_0|^2 =$

1.0×10^{-1} and $|a_2/a_0|^2 = 1.1 \times 10^{-2}$, which are also in good agreement with the experimental results listed in Table I.

IV. CONCLUSION AND OUTLOOK

In conclusion, the emission linewidth of the semiconductor DQD micromaser can be narrowed by more than a factor of 10 using injection locking. Measurements of the injection locking range as a function of input power very closely follow predictions from Adler's theory [19]. We also examined the frequency pull and emission sidebands outside of the injection locking regime. Our data show that this exotic maser, which is driven by single-electron tunneling events, is well described by predictions from conventional laser theory. Future areas of work include the development of a quantitative theory to explain how charge noise impacts the emission peak location and linewidth, steps to improve materials to reduce charge noise, and investigation of the micromaser in the single emitter limit (with one semiconductor DQD in the cavity).

ACKNOWLEDGMENTS

Research at Princeton was funded in part by the David and Lucile Packard Foundation, the National Science Foundation (Grants No. DMR-1409556 and DMR-1420541), and the Gordon and Betty Moore Foundation's EPiQS Initiative through Grant No. GBMF4535.

[1] A. L. Schawlow and C. H. Townes, Infrared and optical masers, Phys. Rev. **112**, 1940 (1958).
[2] T. H. Maiman, Stimulated optical radiation in ruby, Nature (London) **187**, 493 (1960).
[3] D. Kleppner, H. M. Goldenberg, and N. F. Ramsey, Properties of the hydrogen maser, Appl. Opt. **1**, 55 (1962).
[4] D. Kleppner, H. C. Berg, S. B. Crampton, N. F. Ramsey, R. F. C. Vessot, H. E. Peters, and J. Vanier, Hydrogen-maser principles and techniques, Phys. Rev. **138**, A972 (1965).
[5] J. C. Mollier, J. Hardin, and J. Uebersfeld, Theoretical and experimental sensitivities of ESR spectrometers using maser techniques, Rev. Sci. Instrum. **44**, 1763 (1973).
[6] J. L. Hirshfield and V. L. Granatstein, The electron cyclotron maser - An historical survey, IEEE Trans. Microw. Theory Techn. **25**, 522 (1977).
[7] I. V. Konoplev, P. McGrane, W. He, A. W. Cross, A. D. R. Phelps, C. G. Whyte, K. Ronald, and C. W. Robertson, Experimental study of coaxial free-electron maser based on two-dimensional distributed feedback, Phys. Rev. Lett. **96**, 035002 (2006).
[8] A. E. Siegman, *Microwave Solid-State Masers* (McGraw-Hill, New York, 1964).
[9] G. J. Dick and R. T. Wang, Ultra-stable performance of the superconducting cavity maser, IEEE Trans. Instrum. Meas. **40**, 174 (1991).
[10] P.-Y. Bourgeois, N. Bazin, Y. Kersalé, V. Giordano, M. E. Tobar, and M. Oxborrow, Maser oscillation in a whispering-gallery-mode microwave resonator, Appl. Phys. Lett. **87**, 224104 (2005).
[11] M. Oxborrow, J. D Breeze, and N. M. Alford, Room-temperature solid-state maser, Nature (London) **488**, 353 (2012).
[12] A. E. Siegman, *Lasers* (University Science Books, Mill Valley, CA, 1986).
[13] R. Mirollo and S. Strogatz, Synchronization of pulse-coupled biological oscillators, SIAM J. Appl. Math. **50**, 1645 (1990).
[14] S. Kaka, M. R. Pufall, W. H. Rippard, T. J. Silva, S. E. Russek, and J. A. Katine, Mutual phase-locking of microwave spin torque nano-oscillators, Nature (London) **437**, 389 (2005).
[15] S. Hofferberth, I. Lesanovsky, B. Fischer, T. Schumm, and J. Schmiedmayer, Non-equilibrium coherence dynamics in one-dimensional Bose gases, Nature (London) **449**, 324 (2007).
[16] H. L. Stover and W. H. Steier, Locking of laser oscillators by light injection, Appl. Phys. Lett. **8**, 91 (1966).
[17] U. Schünemann, H. Engler, M. Zielonkowski, M. Weidemüller, and R. Grimm, Magneto-optic trapping of lithium using semiconductor lasers, Opt. Commun. **158**, 263 (1998).
[18] Y.-Y. Liu, K. D. Petersson, J. Stehlik, J. M. Taylor, and J. R. Petta, Photon Emission from a Cavity-Coupled Double Quantum Dot, Phys. Rev. Lett. **113**, 036801 (2014).
[19] R. Adler, A study of locking phenomena in oscillators, Proc. IRE **34**, 351 (1946).
[20] J. Jahanpanah and R. Loudon, Theory of laser-amplifier injection locking, Phys. Rev. A **54**, 5210 (1996).
[21] Y.-Y. Liu, J. Stehlik, C. Eichler, M. J. Gullans, J. M. Taylor, and J. R. Petta, Semiconductor double quantum dot micromaser, Science **347**, 285 (2015).
[22] A. Wallraff, D. I. Schuster, A. Blais, L. Frunzio, R.-S. Huang, J. Majer, S. Kumar, S. M. Girvin, and R. J. Schoelkopf, Strong coupling of a single photon to a superconducting qubit using circuit quantum electrodynamics, Nature (London) **431**, 162 (2004).
[23] T. Frey, P. J. Leek, M. Beck, A. Blais, T. Ihn, K. Ensslin, and A. Wallraff, Dipole Coupling of a Double Quantum Dot to a Microwave Resonator, Phys. Rev. Lett. **108**, 046807 (2012).
[24] K. D. Petersson, L. W. McFaul, M. D. Schroer, M. Jung, J. M. Taylor, A. A. Houck, and J. R. Petta, Circuit quantum electrodynamics with a spin qubit, Nature (London) **490**, 380 (2012).
[25] H. Toida, T. Nakajima, and S. Komiyama, Vacuum Rabi Splitting in a Semiconductor Circuit QED System, Phys. Rev. Lett. **110**, 066802 (2013).
[26] G.-W. Deng, D. Wei, J. R. Johansson, M.-L. Zhang, S.-X. Li, H.-O. Li, G. Cao, M. Xiao, T. Tu, G.-C. Guo, H.-W. Jiang, F. Nori, and G.-P. Guo, Charge Number Dependence of the Dephasing Rates of a Graphene Double Quantum Dot in a Circuit QED Architecture, Phys. Re. Lett. **115**, 126804 (2015).
[27] S. Nadj-Perge, S. M. Frolov, E. P. A. M. Bakkers, and L. P. Kouwenhoven, Spin-orbit qubit in a semiconductor nanowire, Nature **468**, 1084 (2010).
[28] W. G. van der Wiel, S. De Franceschi, J. M. Elzerman, T. Fujisawa, S. Tarucha, and L. P. Kouwenhoven, Electron transport through double quantum dots, Rev. Mod. Phys. **75**, 1 (2002).
[29] T. Fujisawa, T. H. Oosterkamp, W. G. van der Wiel, B. W. Broer, R. Aguado, S. Tarucha, and L. P. Kouwenhoven, Spontaneous

emission spectrum in double quantum dot devices, Science **282**, 932 (1998).

[30] M. R. Delbecq, V. Schmitt, F. D. Parmentier, N. Roch, J. J. Viennot, G. Fève, B. Huard, C. Mora, A. Cottet, and T. Kontos, Coupling a Quantum Dot, Fermionic Leads, and a Microwave Cavity on a Chip, Phys. Rev. Lett. **107**, 256804 (2011).

[31] M. R. Delbecq, L. E. Bruhat, J. J. Viennot, S. Datta, A. Cottet, and T. Kontos, Photon-mediated interaction between distant quantum dot circuits, Nat. Commun. **4**, 1400 (2013).

[32] J. Faist, F. Capasso, D. L. Sivco, C. Sirtori, A. L. Hutchinson, and A. Y. Cho, Quantum Cascade Laser, Science **264**, 553 (1994).

[33] D. Meschede, H. Walther, and G. Müller, One-Atom Maser, Phys. Rev. Lett. **54**, 551 (1985).

[34] J. McKeever, A. Boca, A. D. Boozer, J. R. Buck, and H. J. Kimble, Experimental realization of a one-atom laser in the regime of strong coupling, Nature **425**, 268 (2003).

[35] S. Ates, S. M. Ulrich, S. Reitzenstein, A. Löffler, A. Forchel, and P. Michler, Post-Selected Indistinguishable Photons from the Resonance Fluorescence of a Single Quantum Dot in a Microcavity, Phys. Rev. Lett. **103**, 167402 (2009).

[36] The frequency resolution is limited by the resolution bandwidth of the Agilent spectrum analyzer E4405B. For Fig. 3 the RBW is set to 3 kHz and 10 kHz for Fig. 4–6.

[37] M. Armand, On the output spectrum of unlocked driven oscillators, Proc. IEEE **57**, 798 (1969).

[38] H. L. Stover, Theoretical explanation for the output spectra of unlocked driven oscillators, Proc. IEEE **54**, 310 (1966).

[39] M. R. St-Jean, M. I. Amanti, A. Bernard, A. Calvar, A. Bismuto, E. Gini, M. Beck, J. Faist, H. C. Liu, and C. Sirtori, Injection locking of mid-infrared quantum cascade laser at 14 GHz, by direct microwave modulation, Laser Photonics Rev. **8**, 443 (2014).